PCCP

ROYAL SOCIETY OF CHEMISTRY

PAPER

View Article Online
View Journal | View Issue

Cite this: *Phys. Chem. Chem. Phys.*, 2024, **26**, 18102

First-principles prediction of half metallic-ferromagnetism in $La_{0.25}Sr_{0.75}Sn_{0.4}In_{0.25}Ru_{0.35}O_3$ and enhanced experimental electrical and magnetic behaviours†

Samira Barouni,[a] Ameni Brahmia,[b] Hanen Chaker,[a] Mikhail M. Maslov,[c] Akram Alhussein[d] and Rached Ben Hassen *[a]

Received 23rd March 2024,
Accepted 6th June 2024

DOI: 10.1039/d4cp01233j

rsc.li/pccp

A successful mechanochemical synthesis of a new nanoscale semi-conductive perovskite, $La_{0.25}Sr_{0.75}Sn_{0.4}In_{0.25}Ru_{0.35}O_3$ (LSSIRuO) was achieved through co-doping of $SrSnO_3$. XRD and IR analyses confirmed that the sample crystallized in a pure perovskite $GdFeO_3$ type structure (*Pnma* space group). Diffuse reflectance measurements revealed a direct band gap of 1.3 eV, which was significantly narrowed compared to that of $SrSnO_3$ (4.1 eV). The investigation of DFT calculations into the sextenary systems $La_{0.25}Sr_{0.75}[Sn_{0.4}Ru_{0.35}]In_{0.25}O_3$ and $La_{0.25}Sr_{0.75}[Sn_{0.5}Ru_{0.25}]In_{0.25}O_3$ has revealed semiconductor behavior, very close to a semiconductor–semi metal transition. Importantly, Arrhenius-type charge transport was confirmed through a temperature-dependent conductivity study of the sample, showing good electrical conductivity of 3.6 S m^{-1} at 513 K with an activation energy of E_a = 0.19 eV. Furthermore, the compound exhibited ferromagnetic ordering at temperatures lower than 155 K, contrasting the diamagnetic behavior of $SrSnO_3$. The narrower band gap value (1.3 eV) and improved electrical properties of LSSIRuO, in addition to its ferromagnetic characteristics, distinguish it as a promising candidate for applications in optoelectronics, as well as in memory and spintronic devices.

1. Introduction

Tin-based perovskites with general formula ABO_3 have attracted the attention of researchers in the fields of photocatalysis,[1] energy,[2] and gas sensing.[3] One of the key compounds in this stannate family is $SrSnO_3$ (SSO), which stands out due to its structural flexibility, reduced lattice parameters, and high transparency with a wide band gap ranging from 3.9 to 4.5 eV.[4] Compared to conventional binary oxides such as ZnO, In_2O_3, and SnO_2, the perovskite structure of $SrSnO_3$ offers a better control over its optical properties.[5] Visible light absorption is observed in SSO by increasing the doping level, thanks to the orthorhombic distortion of its perovskite structure.[6] The tilting of octahedra in tin-based perovskites is also a crucial factor in determining their physical properties, as slight changes can lead to drastic variations in these properties.[7] $SrSnO_3$ is classified as an n-type material[6] and is used, both doped and undoped, as a humidity sensor. Sensitivity increases with donor substitution, while electrical conductivity is enhanced in acceptor-doped $SrSnO_3$.[8] To meet the growing demand for high-performance oxides in multiple applications with commercial viability, $SrSnO_3$ is often doped with alkali metals, transition metals, post-transition elements, and rare earth elements, either on the A-site, B-site, or simultaneously on both sites. Thus tuned new obtained materials could present innovative properties by enhancing or refining characteristics such as thermal stability, chemical stability, electrical conductivity, magnetic effects, catalytic activity, and electrolytic compatibility.[9,10]

According to the literature, A-site doping of $SrSnO_3$ with lanthanum (La) has been observed.[7] Lanthanum is a rare earth element known for its ability to retain parent crystal structures and promote electrical conductivity.[11] Furthermore, ruthenium (Ru), a transition metal with good catalytic and magnetic properties, as well as excellent chemical stability, is often used as a substitute to enhance the activity and selectivity of catalytic materials.[12] Indium (In) is well known as a dopant in

[a] *Laboratory of Materials and Environment for Sustainable Development (LR18ES10), University of Tunis El Manar, Tunisia. E-mail: rached.benhassen@issbat.utm.tn*
[b] *Department of Chemistry, College of Science, King Khalid University, P.O. Box 9004, 61413 Abha, Saudi Arabia*
[c] *Nanoengineering in Electronics, Spintronics and Photonics Institute, National Research Nuclear University "MEPhI", Kashirskoe Shosse 31, Moscow 115409, Russia*
[d] *LASMIS, Université de Technologie de Troyes, Pôle Technologique Sud Champagne, 26 rue Lavoisier, Nogent 52800, France*

† Electronic supplementary information (ESI) available. See DOI: https://doi.org/10.1039/d4cp01233j

semiconductors often used in electronics, optics and solar cells due to its ability to improve electrical conductivity and form thin films.[13] Thus, the selection of these substitutes La, Ru and In in the new material has the essential objective of contributing to improving the performance and characteristics of the material for some intended applications.

Significant efforts have been dedicated to the development of highly efficient and air-stable tin-based perovskite solar cells.[14,15] In this context, an intriguing alternative as a light absorber for lead-free solar cells is $CsSnI_3$, with a band gap of 1.3 eV,[15] a low excitonic binding energy of 18×10^{-3} eV,[16] and a high optical absorption coefficient of 10^4 cm^{-1} (comparable to that of $MAPbI_3$).[16] Nevertheless, it is imperative to overcome the major challenge related to the instability of $CsSnI_3$, as its black phase tends to easily transform into a yellow phase after oxidation in the atmosphere.[16] The preferred solution in this case is the development of new tin-based perovskite oxides due to their advantages, such as greater stability than halide-based perovskites or halide-based hybrid perovskites. In addition, they exhibit better optical absorption in the visible range than halides.[16]

The exploration of ferromagnetic half-metallic materials is crucial due to their potential applications in memory and spintronic devices. In order to develop new promising candidates for achieving half-metallic ferromagnets (HMFs),[17] several attempts were carried out by substituting B-site ions in $SrRuO_3$ with Ti^{4+} and Sn^{4+} to explore transforming of a simple ferromagnetic metal, into a half-metal.[18–21] Despite theoretical advances in the search for new HMFs, the experimental realization of these materials remains challenging. The few well-established examples of half-metallic ferromagnetism were materials adopting a double perovskite type structure,[22] where a double-exchange mechanism leading to a half-metallic state with associated magnetic properties should be expected as suggested by J. H. Park *et al.*[23] The transition from double perovskite systems to simple perovskites to achieve ferromagnetic half-metallicity is motivated by the stringent constraints of B-site ordering in the former.[20]

In this study, we report the structure as well as the electrical, magnetic and optical properties of $SrSnO_3$ (perovskite oxide) doped with La, Ru and In. To date, no experimental studies or DFT analyzes exist on how the co-doping of In and Ru systematically influences the electronic and magnetic properties of $SrSnO_3$, whether in bulk or in thin film form.

2. Experimental and theoretical section

2.1 Synthesis of $La_{0.25}Sr_{0.75}Sn_{0.4}In_{0.25}Ru_{0.35}O_3$

The synthesis of LSSIRuO powder employed the eco-friendly mechanosynthesis method, known for its simplicity and cost-effectiveness. This is achieved through the use of affordable starting materials and the omission of solvents, effectively addressing waste disposal concerns. Moreover, mechanosynthesis provides a versatile and efficient approach, affording control over composition and properties. In this particular process, precise amounts of La_2O_3 (99.9+%; Sigma-Aldrich), $SrCO_3$ (99.9+%; Sigma-Aldrich), SnO_2 (99.9%; Alfa), RuO_2 (99.9%; Sigma-Aldrich) and In_2O_3 (99.9%; Sigma-Aldrich) precursors, with purity exceeding 99.9%, were dried and weighed using a high-precision balance. The weighed precursors were then introduced into the mill (FRITSCH GmbH), and ground for 3 hours at a speed of 500 rpm, with a ball-to-precursor ratio of 20 : 2. After the initial grinding, a second grinding step was carried out, followed by calcination at 950 °C and subsequent XRD diffraction analysis. Based on the presence of diffraction lines corresponding to the SnO_2 precursor, the calcination temperature was increased to 1000 °C for 12 hours. Subsequently, through XRD analysis, it was observed that the intensity of the SnO_2 lines decreased, prompting a further sintering cycle at 1050 °C. This led to the disappearance of the lines associated with the aforementioned precursor. All heating processes were conducted in the presence of air. The stoichiometric proportions of the reagents used in the synthesis are represented by the following equation:

$$\frac{1}{8}La_2O_3 + \frac{3}{4}SrCO_3 + \frac{2}{5}SnO_2 + \frac{7}{20}RuO_2 + \frac{1}{8}In_2O_3 \rightarrow La_{0.25}Sr_{0.75}Sn_{0.4}In_{0.25}Ru_{0.35}O_3 + \frac{3}{4}CO_2$$

2.2 Characterization

Powder X-ray diffraction (XRD) measurements were conducted using an X'Pert3 powder PANalytical diffractometer equipped with Cu Kα radiation (λ = 0.15406 nm). The experimental parameters were carefully set to ensure accurate data acquisition, including a step size of 0.013° and an accumulation time of 30 seconds. The 2θ range covered was from 10° to 110°, and the measurements were performed in a continuous scan mode.

For the analysis of the obtained XRD data, Rietveld refinement was conducted following the established methodology described by Rodriguez-Carvajal in the FullProf program.[24]

To accurately determine the instrumental line broadening, a standard microcrystalline powder was utilized, and its XRD pattern was recorded under identical experimental conditions. This reference measurement served as a benchmark for evaluating and accounting for any broadening effects inherent to the XRD instrument itself.

High-resolution scanning electron microscopy (SEM) measurements were conducted using a cutting-edge FE-SEM instrument (Hitachi SU8030) operating at 10 kV. This advanced SEM instrument allowed us to capture detailed images of the sample surface, providing valuable insights into its microstructure and morphology. Additionally, energy-dispersive X-ray analysis (EDX) was performed using an Oxford INCA x-act system at an acceleration voltage of 15 kV. The EDX analysis enabled the determination of the elemental composition of the sample. Importantly, the analytical errors associated with the elemental content were found to be less than 5 atomic percent (at%), ensuring high accuracy. Quantification of the elements was achieved using the Proza algorithm (Phi-Rho-Z), a reliable method for elemental analysis.

Infrared (IR) measurements were realized using a highly precise spectrometer, BRUKER "TENSOR 27," covering a spectral range from 4000 to 400 cm^{-1}. For the measurements,

approximately 1 mg of the sample was mixed with 300 mg of potassium bromide (KBr) and ground in an agate mortar. The resulting mixture was then pressed into pellets under a pressure of 10 bar.

Diffuse reflectance (DR) spectra were obtained using a UVD-3500 UV-Vis spectrophotometer equipped with a $BaSO_4$-coated integrating sphere. The spectral range covered wavelengths from 190 to 900 nm, with measurements taken at 1 nm intervals. The use of an integrating sphere ensured accurate and reliable measurement of the diffuse reflectance properties of the sample. By analysing the DR spectra, valuable information about the optical properties, such as band gap energy and light absorption behaviour, could be obtained, contributing to a comprehensive characterization of the material.

For the theoretical geometry optimization and study of the electronic structure and optical properties of LaSrSnInRuO compound, we employed the implementation of density functional theory (DFT) calculations in the QUANTUM Espresso 6.5 program package.[25,26] The plane-wave basis set for valence electron states with the cutoff energy of 120 Ry (1632 eV), corresponding to 800 Ry (10 880 eV) for the charge density cutoff, was taken. We considered the Perdew–Burke–Ernzerhof (GGA-PBE) functional for the description of exchange–correlation energy.[27] Pseudopotentials for the electronic structure calculations were taken from the standard solid-state pseudopotentials (SSSP) library.[28,29] The projector-augmented-wave (PAW) method for the electron–ion interaction[30,31] was also applied to perform the numerical simulation. To take into account the magnetic order in the LaSrSnInRuO compound we used the generalized gradient spin approximation (GGSA). The calculations were performed within the Hubbard-corrected DFT energy functionals (GGSA+U) for the ruthenium atoms. The GGSA+U approach[32–34] can overcome the lack of a DFT-based correlation–exchange functional by combining DFT with the Hubbard model. To consider the strong correlation induced by Ru 4d electrons, an on-site Coulomb interaction U = 5.0 eV is chosen in GGSA+U calculations. The Brillouin zone integrations were performed using the Monkhorst–Pack k-point sampling scheme[35] with the $4 \times 4 \times 4$ mesh grid (for the non-self-consistent field calculations, the k-point grid size of $8 \times 8 \times 8$ was used) together with the Methfessel–Paxton smearing[36] with the smearing width of 0.02 Ry. For the calculations of the electronic density of states, the Böchl tetrahedron method[37] was employed. Periodical boundary conditions were used. The atomic equilibrium positions were obtained by the complete minimization of the unit cell using the calculated forces and stress on the atoms. The convergence criterion of self-consistent calculations for ionic relaxations is 10^{-8} eV between two consecutive steps. Furthermore, all atomic positions and the supercell itself were optimized until all components of all forces acting on the atoms became smaller than 10^{-4} hartree per Bohr. Such criteria ensure that the absolute value of stress is less than 0.01 kbar. The electronic structure properties were elucidated by analyzing the sample band structure and its electronic density of states. In order to get the accurate band gaps, the beyond GGA methods such as Gaussian attenuating Perdew–Burke–Ernzerhof (Gau-PBE) that uses a Gaussian function as a modified Coulomb potential for the exact exchange,[38] and Heyd–Scuseria–Ernzerhof (HSE) hybrid functional approaches[39] were included. The use of these approaches allowed us to refine the values of band gaps.

Direct current electrical measurements were conducted using a Lucas Labs S-302 four-point probe and a Keithley 2400 digital source counter (Keithley Instruments, Inc., Cleveland, Ohio). The measurements were performed over a temperature range of 330–520 K. The sample used for the measurements had a diameter of 8 mm and a thickness of 2 mm.

To investigate the magnetic properties of the samples, a MANICS DSM-8 differential magneto-susceptometer was employed. The measurements were carried out under an applied magnetic field of up to 1.5 T. The magnetization of the samples was measured using two modes: FC (field-cooled) and ZFC (zero-field-cooled). Additionally, hysteresis measurements were performed for a deeper understanding of the magnetic properties exhibited by the samples.

3. Results and discussion

3.1 Structural analysis

3.1.1 Crystal structure and phase determination. A qualitative analysis using X-ray powder diffraction, followed by identification using the ICDD PDF4+ database, confirmed the presence of a new phase, while no traces of the precursor materials were detected. The structural investigation of the developed material was conducted using the Rietveld method, adopting the perovskite structure type of $GdFeO_3$ (space group *Pnma*).

The crystallographic parameters derived from this analysis are presented in Table 1, providing valuable insights into the structural characteristics of the material. Fig. 1 illustrates the profiles obtained from the Rietveld refinement process, including the observed, calculated, and difference profiles. Additionally, Fig. 1 presents the structure of the LSSIRuO compound. It is noteworthy that nearly all reflections are successfully indexed. The refinement results and atomic positions are presented in Table 1. The stability of this structure is supported by three well-established factors: the Goldschmidt tolerance factor[40] t, the octahedral factor[41] μ and the newly introduced tolerance factor[42] τ.

The formulas for these factors are presented in equations (eqn (1)–(3)), and their corresponding values are illustrated in Table 2. In these expressions, r(A) and r(B) represent the Shanon ionic radii[43] of A (Sr^{2+} or La^{3+}) and B (Sn^{4+}, In^{3+}, or Ru^{4+}), respectively, while n_A denotes the oxidation state of A. The ionic radii, considering a coordination of twelve for (Sr, La), six for (Sn, In, and Ru), and two for oxygen, are as follows: $r(O^{2-})$ = 1.4 Å, $r(Sr^{2+})$ = 1.44 Å, $r(La^{3+})$ = 1.36 Å, $r(Sn^{4+})$ = 0.69 Å, $r(In^{3+})$ = 0.8 Å, and $r(Ru^{4+})$ = 0.62 Å.[43]

$$t = \frac{0.25 \times r(La^{3+}) + 0.75 + r(Sr^{2+}) + r(O^{2-})}{\sqrt{2} \times (0.4 \times r(Sn^{4+}) + 0.25 \times r(In^{3+}) + 0.35 \times r(Ru^{4+}) + r(O^{2-}))} \quad (1)$$

$$\mu = \frac{r_{(B)}}{r_{(O)}} \quad (2)$$

Table 1 Crystallographic data and structural parameters of $La_{0.25}Sr_{0.75}Sn_{0.4}In_{0.25}Ru_{0.35}O_3$

Temperature	300 K
Chemical formula	$(La_{0.25}Sr_{0.75})(Sn_{0.4}In_{0.25}Ru_{0.35})O_3$
Formula weight (M)	844.023 g mol^{-1}
Space group	*Pnma* (no. 62)
Lattice parameters	
a (Å)	5.6848(8)
b (Å)	8.0676(8)
c (Å)	5.6961(10)
V (Å^3)	261.24(6)
Z	4
χ^2	1.84
R_p	2.72
$R_{Expected}$	2.57
R_{wp}	3.49
R_I	2.02
D_{W-H} (nm)	98
D_{MEB} (nm)	135
Strain	0.0095

Atomic positions

Atoms	Sites	Occupancy	X	Y	Z	U_{iso}
La	4c	0.25	0.0024	0.2500	0.4962	0.0320(9)
Sr	4c	0.75	0.0024	0.2500	0.4962	0.0320(9)
Ru	4a	0.35	0.0000	0.0000	0.0000	0.0087(6)
In	4a	0.25	0.0000	0.0000	0.0000	0.0087(6)
Sn	4a	0.40	0.0000	0.0000	0.0000	0.0087(6)
O_1	8d	1.00	0.2825	0.0342	0.2154	0.01312
O_2	4c	1.00	0.4891	0.2500	0.5666	1.03989

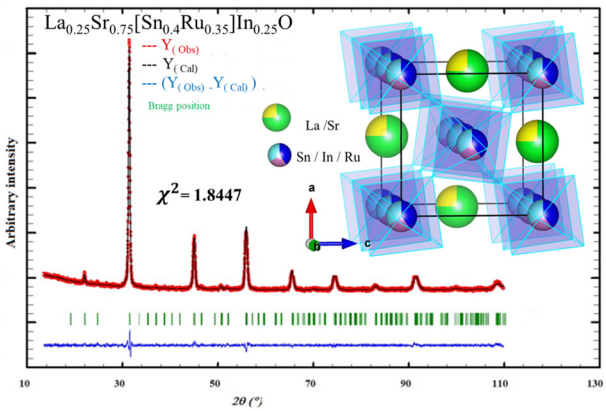

Fig. 1 Observed, calculated and difference of X-ray diffraction patterns of $La_{0.25}Sr_{0.75}Sn_{0.4}In_{0.25}Ru_{0.35}O_3$ powder calcined at 1050 °C with structure inset.

$$\tau = \frac{r_{(O)}}{r_{(B)}} - n_A\left(n_A - \frac{\frac{r_{(A)}}{r_{(B)}}}{\ln\frac{r_{(B)}}{r_{(O)}}}\right) \quad (3)$$

These factors provide further confirmation of the stability of the structure in the orthorhombic system.

This structure consists of interconnected $(Sn/In/Ru)O_6$ octahedra at the corners, with each Sn, In, or Ru surrounded by six oxygen ions. These octahedra are adjacent to large $(La/Sr)O_9$ cavities. In this orthorhombic structure, all B cations occupy the same crystallographic site 4a (0, 0, 0), while the A cations reside in 4c. The two oxygen atoms, O_1 and O_2, occupy non-equivalent crystallographic sites, 8d and 4c, respectively. Surrounding each oxygen, there are 2 Sn^{4+} ions and 4 Sr^{2+} ions, forming octahedral coordination environments. The Sn–O_1 distances range from 2.0394(2) Å to 2.0576(2) Å, with an average of 2.0485 Å. The Sn–O_2 distance is 2.0532(2) Å, resulting in an average Sn–O bond length of 2.0501 Å, which is slightly smaller than the average value in $SrSnO_3$ (2.0504 Å).[7] The Sr–O bond lengths vary between 2.4590(2) Å and 2.9455(5) Å, with an average value of 2.7352 Å, compared to 2.8685 Å in $SrSnO_3$ and related compounds.[7,44] These bond lengths fall within the typical range observed in octahedral environments.[45,46] With doping, the covalency of the bonds increases, resulting in a slight decrease in the average Sn–O and Sr–O bond lengths. The values of the Sn–O_1–Sn and Sn–O_2–Sn angles (θ_1 and θ_2, respectively) are 158.276(4)° and 158.420(2)°, respectively, which are consistent with the findings of Mizoguchi *et al.*[47] In $SrSnO_3$, these values are Sn–O_1–Sn = 160.73° and Sn–O_2–Sn = 158.60°.[7] Using the mathematical relations (eqn (4)) proposed by O'keeffe *et al.*,[7,48] which established the connection between these angles and the tilting angles, we calculated the tilt in our material, resulting in an average value of 13.242°, compared to 12.44° in $SrSnO_3$.[7]

$$\cos\theta_1 = \frac{1-4(\cos\varphi_1)^2}{3} \quad \cos\theta_2 = \frac{2-5(\cos\varphi_2)^2}{2+(\cos\varphi_2)^2} \quad (4)$$

The difference between these two values of ~1°, is not significant to induce a big change in symmetry, indeed the orthorhombic symmetry is still maintained in our structure. These tilt values align well with the tolerance factor t being less than 1.

The relationship between octahedral rotations and the covalent nature of metal–oxygen bonds in orthorhombic perovskites was explored by Cammarata *et al.*[49] Their research indicated that the covalency of the metal–oxygen bond influenced the degree of octahedral rotation, with a less covalent B–O bond resulting in a more distorted structure. Consequently, co-doping with less electronegative atoms (Ru, In) is expected to enhance the conduction bandwidth and reduce the band gap, which will be verified through UV-Vis spectroscopy in next paragraphs and DFT calculations.

3.1.2 Crystallite size and strain determination. The average grain size, denoted as D, and micro strain in the sample were assessed using the Williamson–Hall (W–H) method (eqn (5)). This method takes into account two factors contributing to the broadening of diffraction peaks, size and deformation.

$$\beta\cos\theta = \left(\frac{K\lambda}{D}\right) + 4\varepsilon\sin\theta \quad (5)$$

In the equation, D and ε represent the crystallite size and microstrain value, respectively, while β corresponds to the half-height width of the diffraction peak, measured in radians (FWHM), and corrected by the instrumental half-height width β (inst). The X-ray wavelength, λ, is 1.54056 Å, and θ denotes the

Table 2 Goldschmidt tolerance factor (t), octahedral factor (μ), and tolerance factor (τ) for $La_{0.25}Sr_{0.75}Sn_{0.4}In_{0.25}Ru_{0.35}O_3$

	t	μ	τ
LSSIRuO	0.9478	0.4928; 0.5714; 0.4428	3.3947
Tolerated values in the perovskite structure	$0.825 < t < 1$	$0.414 < \mu < 0.732$	$\tau < 4.18$

Bragg diffraction angle. The analysis was conducted on 8 lines with intensities exceeding 10% of the maximum intensity, whereas lines at high angles, where measurement errors are more significant, were excluded. By plotting "$\beta \cos\theta$" on the y-axis and "$4 \sin\theta$" on the x-axis, the average crystallite size and microstrain can be estimated by extrapolating the y-intercept and slope of the line (Fig. 2).

The line in the Fig. 2 passes through nearly all points, suggesting a microstructural homogeneity. Additionally, according to the Hume-Rothery crystallographic defect model,[50] the ionic radius difference between the dopant and host cation should be less than 15% to form a stable crystalline system. In the present case, the ionic radius of the dopant In^{3+} (0.8 Å) is 15% higher than that of the host cation Sn^{4+} (0.69 Å), the ionic radius of the dopant Ru^{4+} (0.62 Å) is 10% smaller than that of the host cation Sn^{4+}, while the ionic radius of the dopant La^{3+} (1.36 Å) is 6% higher than that of the host cation Sr^{2+} (1.44 Å). This likely rules out the possibility of oxygen vacancy formation[5] and the incorporation of In, Ru, and La in both cationic sites. The calculated average size is found to be D = 98 nm, while the microstrain is on the order of ε = 0.0095, confirming the nanoscale nature of the particles as shown in Table 1.

3.1.3 Scanning electron microscopy and energy-dispersive X-ray analysis of $La_{0.25}Sr_{0.75}Sn_{0.4}In_{0.25}Ru_{0.35}O_3$. We utilized scanning electron microscopy (SEM) to delve into the surface morphology of LSSIRuO, as depicted in Fig. 3. The micrograph illustrates that particle agglomeration manifests randomly, yielding a diverse array of shapes ranging from 100 nm to 180 nm in size. After fitting the data to a Gaussian function, we determined the average agglomerate size to be 135 nm (Fig. 3). At a relatively high temperature of 1050 °C, a majority of particles undergo agglomeration and consolidation, resulting in a wide size distribution, in accordance with sintering theory.[51] This distribution pattern is reflected in the observed agglomerate sizes. The average particle size (r_{SEM}) was assessed at 135 nm, whereas the minimum crystallite size ($r_{X\text{-ray}}$), calculated from X-ray diffraction (XRD) data, was determined to be 98 nm. Through the relationship $N = r_{SEM}/r_{X\text{-ray}}$, we calculate the number of coherent diffraction domains within a particle. The results indicate that, on average, a particle comprises no more than 1.37 coherent diffraction domains.

To evaluate the chemical purity and elemental composition of LSSIRuO, we employed energy-dispersive spectroscopy (EDS). The EDS analysis confirmed the presence only of the anticipated elements, including La, Sr, Sn, In, Ru, and O, demonstrating the elemental homogeneity of the material and the absence of any foreign elements (Fig. 4). Furthermore, the mass, atomic, theoretical (based on the empirical formula), and experimental (from EDS) percentages within the unit cell of the perovskite LSSIRuO are determined and presented in Table 3. The rather remarkable coincidence between these values and estimates and their agreement and provide information on the chemical coherence of the material.

3.2 Optical properties

3.2.1 Infra-red analysis. The IR absorption spectrum as a function of wavenumber of the studied sample, LSSIRuO, in the range of 4000 to 400 cm^{-1}, is presented in Fig. 5.

The strong band at 663 cm^{-1} may be associated with various O–M–O bends and M–O stretch in the octahedra of InO_6, SnO_6, and RuO_6. As per the literature, the stretching and bending

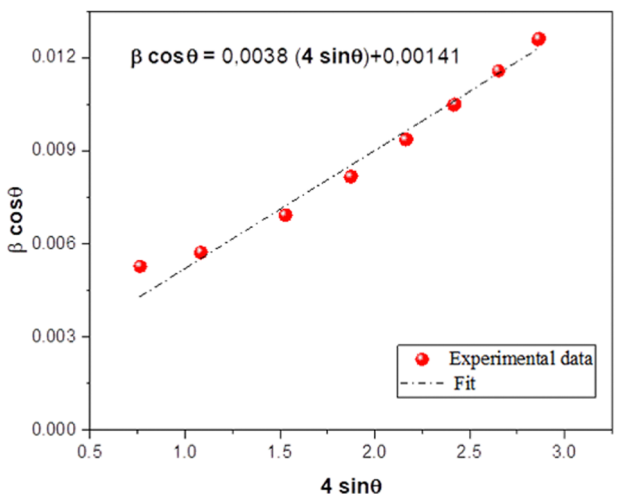

Fig. 2 Williamson–Hall (W–H) plot of $La_{0.25}Sr_{0.75}Sn_{0.4}In_{0.25}Ru_{0.35}O_3$.

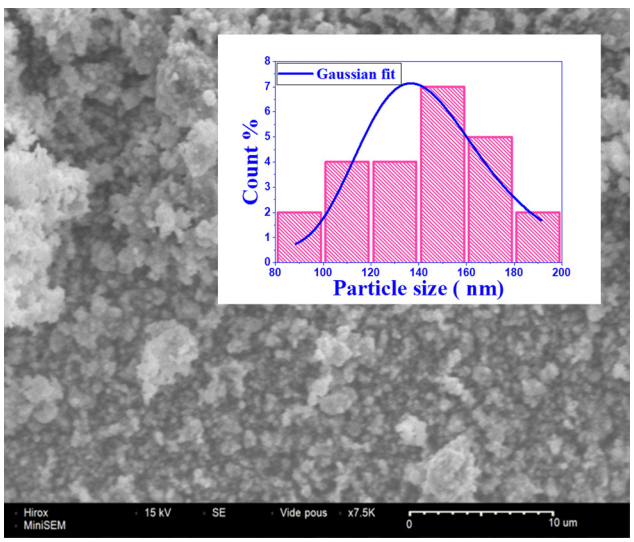

Fig. 3 SEM image and grain size histogram of $La_{0.25}Sr_{0.75}Sn_{0.4}In_{0.25}Ru_{0.35}O_3$.

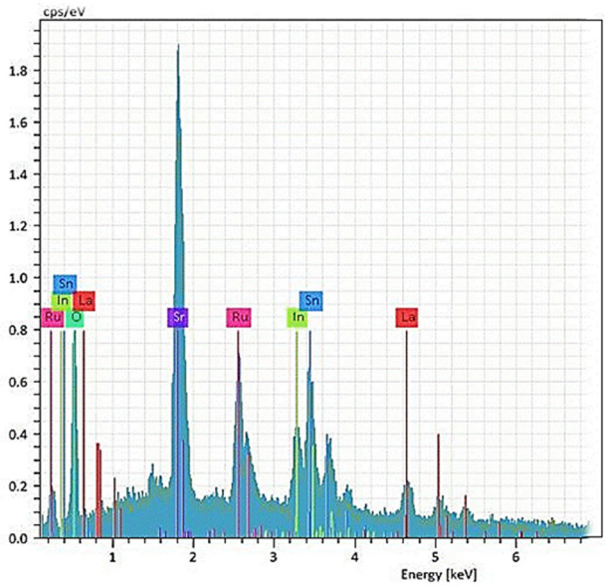

Fig. 4 EDS spectrum of $La_{0.25}Sr_{0.75}Sn_{0.4}In_{0.25}Ru_{0.35}O_3$.

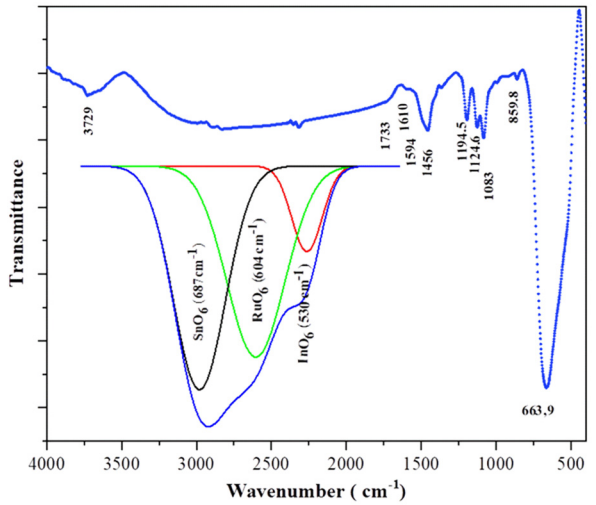

Fig. 5 FTIR spectrum of $La_{0.25}Sr_{0.75}Sn_{0.4}In_{0.25}Ru_{0.35}O_3$ and deconvolution of the spectral band at 663 cm^{-1}.

vibrations of SnO_6 are typically identified between 624 and 687 cm^{-1}.[52] Those corresponding to the In–O bonds within InO_6 octahedra are commonly observed within the range of 405 to 560 cm^{-1}.[4,52] In the case of ruthenates, the absorptions linked to the stretching and bending of the Ru–O bond are reported to be located between 414 cm^{-1} and 524 cm^{-1} with weak intensity.[53] The deconvolution of this broad band that spreads from 500 to 800 cm^{-1}, using Gaussian function, gives three absorption peaks, shown in Fig. 5 to characterize the various O–M–O bends and M–O stretch (with M being Sn, In or Ru). In addition to the metal–oxygen bands, vibrations attributed to carbonates, water, and the Sn–OH bond are also observed. The carbonate can be formed by the absorption of atmospheric CO_2 or, alternatively, it can be derived from the strontium carbonate used as a starting precursor in the solid-state synthesis.[54] If carbonate is trapped in the perovskite structure, it would replace the O^{2-} anions and is bound to Sr^{2+}. The presence of these carbonates in the perovskite lattice leads to greater disorder in the $(Sn/In/Ru)O_6$ octahedra. Nyquist and Kagel showed that carbonate bands are located at 1320–1530, 1040–1100, and 800–890 cm^{-1}.[55] Our compound exhibits bands around 1456, 1083, and 860 cm^{-1}. The presence of water is probably observed due to its adsorption by LSSIRuO as SrO is a hygroscopic oxide.[56] The broad band located between 3450 and 3900 cm^{-1} is probably due to the stretching vibration of the hydroxyl group O–H (free and bound). This presence is confirmed by a weak band around 1627 cm^{-1}, which is caused by the bending vibration of H_2O and Sn–OH.[57] This OH group may also be bound, in addition to water and Sn, to oxygen atoms on the surface.

Table 3 Theoretical and experimental mass and atomic percentages

The theoretical mass and atomic percentages			The experimental mass and atomic percentages		
Element	Mass (%)	Atom (%)	Mass (%)	Atom (%)	Absolute error (%)
Strontium	25.27	15	25.48	14.61	0.99
Oxygen	18.46	60	19.80	62.17	3.77
Tin	18.26	8	17.72	7.50	0.65
Lanthanum	13.35	5	13.15	5.51	0.70
Ruthenium	13.6	7	11.55	5.74	0.45
Indium	11.04	5	10.21	4.47	0.42

3.2.2 UV-Visible analysis. The Kubelka–Munk function $F(R)$, expressed by the formula:

$$F(R) = (1 - R)^2/2R = K/S \quad (6)$$

with R as reflectance, K as absorption coefficient and S as backscatter coefficient, indicates, as shown in Fig. 6(a) that LSSIRuO exhibits absorption over the entire wavelength spectrum, in the case where we assume that the radiation moves through layers of infinitesimal size.

This was facilitated by the common hypothesis that the Kubelka–Munk function was analogous to the absorbance function in transmission spectroscopy.

To determine the optical band gap of LSSIRuO, the Tauc method was employed, using the relation $(F(R)\cdot h\nu)^p = A(h\nu - E_g)$. Here, E_g represents the band gap energy, A is a constant, and p is the index that can take on various values (1/2, and 2) corresponding to indirect allowed and direct allowed transitions, respectively. We graphed the Tauc relation with various exponents against $h\nu$ to precisely determine the optical band gap. The analysis disclosed an E_g value of 1.3 eV in Fig. 6(b), indicating a direct allowed transition as illustrated in Fig. 6(c). Remarkably, the band gap showed a significant decrease with La, In, and Ru doping compared to pure $SrSnO_3$, which had a band gap of 4.1 eV,[10] $Sr(Ru, Sn)O_3$ with 0.4 eV,[20] $Sr(In, Sn)O_3$ with 3.8 eV[58] and $(La, Sr)SnO_3$ with 3.97 eV.[7]

It is noteworthy that this band gap is smaller than those of $CH_3NH_3PbBr_3$ (2.26 eV) and $CH_3NH_3PbCl_3$ (3 eV), but of the same order as that of $CH_3NH_3BiSeI_2$, $MASnI_3$, and $CsSnI_3$.[16] These findings highlight the potential of this simple oxide

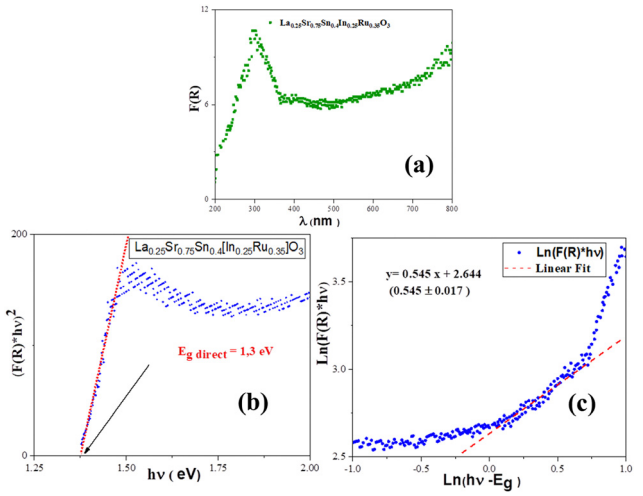

Fig. 6 (a) Kubelka–Munk function $F(R)$ for $La_{0.25}Sr_{0.75}Sn_{0.4}In_{0.25}Ru_{0.35}O_3$ as a function of wavelength λ. (b) Tauc plot for $La_{0.25}Sr_{0.75}Sn_{0.4}In_{0.25}Ru_{0.35}O_3$. (c) Plot of $\ln(F(R) \times h\nu)$ *vs.* $\ln(h\nu - E_g)$.

perovskite semiconductor as an environmentally friendly alternative to lead halide-based perovskite semiconductors.

3.3 Density functional theory calculations

To study the electronic properties of the LSSIRuO compound, we analyze the electronic characteristics, namely band structure and density of electronic states of the sample's equilibrium structure. The total density of states (DOS) and the band structure along high symmetry directions of the optimized sample are shown in Fig. 7(a). The Fermi level is set to zero energy.

The nature of the electronic band structure and the density of states indicate that the LSSIRuO sample exhibits metallic nature. The finite value of the density of electronic states at the Fermi level and the absence of the explicit dielectric gap indicate that the LSSIRuO belongs to the class of semi-metals or even metals. Additional analysis of the partial density of electronic states (PDOS, Fig. 7(b)) demonstrates that the number of states at the Fermi level in the conduction band is primarily composed of ruthenium and oxygen atoms. Thus, the GGA approximation predicts the absence of energy gap at the Fermi level. It should be noted that taking into account the magnetic order in the LaSrSnInRuO compound using the generalized gradient spin approximation (GGSA) and within the framework of the Hubbard model (U = 5.0 eV) indicates the presence of a semiconductor gap in the sample. The nature of the density of electronic states in this case indicates that the LaSrSnInRuO sample exhibits the semiconducting properties (see Fig. 8). The density of electronic states is equal to zero at the Fermi level and possesses a gap. An estimation of the band gap at the GGSA+U level of theory gives the value of 1.55 eV, which agrees well with the experimentally obtained value of 1.3 eV.

Adjusting the substitution ratio of Sn by Ru and increasing the Sn content to 0.5 in our formulation, corresponding to a Sn to Ru ratio of x = 0.66, results in the compound

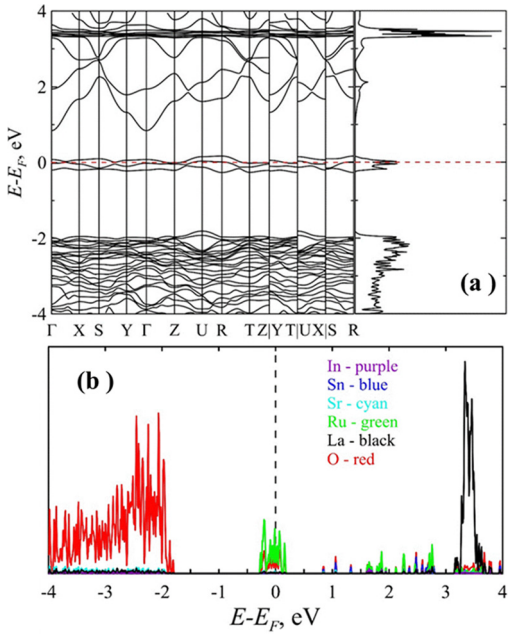

Fig. 7 (a) Band structure and density of electronic states of the $La_{0.25}Sr_{0.75}Sn_{0.4}In_{0.25}Ru_{0.35}O_3$ material. Γ, X, S, Y, Z, U, R, and T are the standard notations for the high-symmetry characteristic points in the Brillouin zone, where Γ corresponds to the center of the Brillouin zone. The Fermi level is assigned at zero. (b) Partial density of electronic states for the $La_{0.25}Sr_{0.75}Sn_{0.4}In_{0.25}Ru_{0.35}O_3$ sample. The Fermi level is assigned at zero.

$La_{0.25}Sr_{0.75}Sn_{0.5}In_{0.25}Ru_{0.25}O_3$, which, according to our DFT results, exhibits semiconductor behavior with a gap of 0.75 eV (Fig. 9). It should be noted that GGA level of theory tends to underestimate the dielectric gap. So, we made a refinement using the Gau-PBE and HSE hybrid functional. The HSE approach gives an estimate of 11.69 eV for the bottom of the conduction band and 9.69 eV for the top of the valence band. Thus, the determined band gap using the HSE approach is equal to 2 eV, which corresponds to a value more characteristic of a semiconductor. Data obtained within the framework of the Gau-PBE approach confirm this result. The estimated semiconductor gap in this case is 1.93 eV. Increasing tin content leads to a shift in the Fermi level, and a gap appears.

This finding agreed well with the detailed experimental study on the effects of Sn substitution in $SrRuO_3$ done by Amand *et al.*[21] in which they classified all the compositions with $x > 0.44$ as semiconductors or even insulators.

On the other hand, calculations with LSDA (local spin-density approximation) and LSDA+U method led by Kim *et al.*[20] showed that Ru's electron hopping 'd' is blocked by Sn-substituted sites, resulting in a reduction of the Rut2g bandwidth as doping x increases. Transitions from ferromagnetic metal (FM) to ferromagnetic half-metal (HMF) up to the insulator are described by the Rut2g bandwidth (W), the position of the maximum valence band (Δ) in the majority spin channel, and the band gap. The HMF region is observed for $0.5 \leq x \leq 0.7$, with a potential half-metal-to-insulator transition at $x \approx 0.7$. It is noteworthy that our compound's doping ratio (Sn/Ru) x = 0.53 falls within the semiconductor region

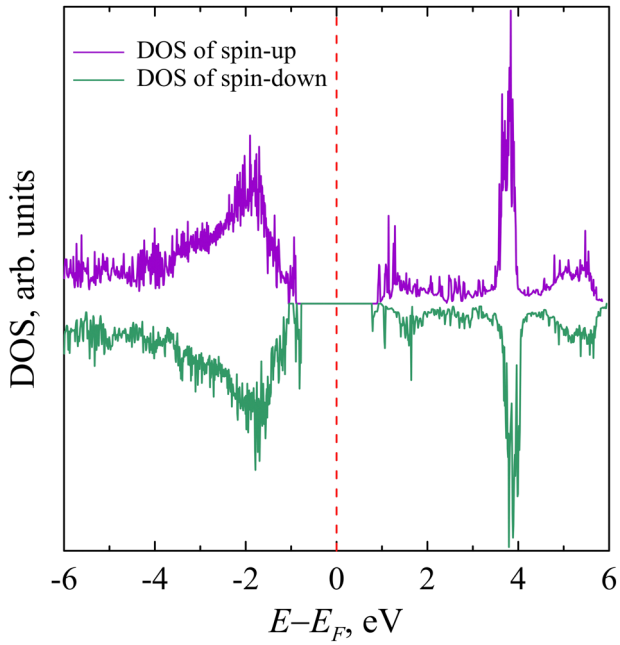

Fig. 8 The density of electronic states of the LaSrSnInRuO sample obtained at the GGSA+U approach. The Fermi level is assigned at zero.

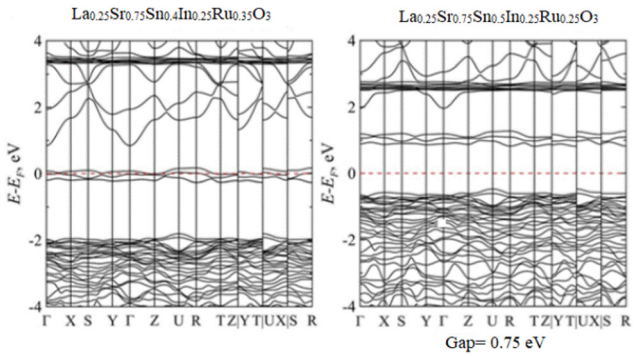

Fig. 9 Band structures and density of electronic states of $La_{0.25}Sr_{0.75}Sn_{0.4}In_{0.25}Ru_{0.35}O_3$ and $La_{0.25}Sr_{0.75}Sn_{0.5}In_{0.25}Ru_{0.25}O_3$.

close to the HMF region. Probably, by decreasing the Sn content in our formulation, we could reach the half-metal to insulator transition.

3.4 Electrical properties

The electrical properties of the sample were analyzed by studying the electrical conductivity as a function of temperature. It is well established that the dc conductivity of the sample is related to temperature according to Arrhenius equation (eqn (7))

$$\sigma_{dc} = \sigma_0 \exp\left(\frac{-E_a}{k_B T}\right) \quad (7)$$

Here, σ_0 represents the pre-exponential factor, k stands for the Boltzmann constant, and E_a denotes the activation energy necessary for the mobility of charge carriers in the sample. The Arrhenius plot depicting samples with $\ln \sigma_{(dc)}$ *vs.* $1000/T$ is presented in Fig. 10. The linear correlation observed between values of $\log \sigma_{(dc)}$ *vs.* $1000/T$ strongly indicates Arrhenius-type conduction in the sample. Within 333–513 K temperature range, a singular conduction process prevails in the LSSIRuO sample, characterized by an activation energy of 0.19 eV. Such a low activation energy value of LSSIRuO sample could suggest a more favored ionic conduction process within degenerate sites of (Sn^{4+}/Sn^{2+}) and (Ru^{4+}/Ru^{3+}).[59]

For instance, the dc conductivity shows a 100-fold increase from 3.2 10^{-2} S m^{-1} at 333 K to 3.6 S m^{-1} at 513 K. This improvement in conductivity is expected for several reasons:

(i) Doping perovskite oxides with trivalent (3+), such as La^{3+}, is known to enhance their electrical properties.[7]

(ii) Substituting La^{3+} for Sr^{2+} creates a mixed valence state of Sn^{2+}–Sn^{4+}, Ru^{4+}–Ru^{3+} generating mobile charge carriers. This process strongly influences electrical conductivity, with sensitivity to chemical composition and oxygen content.[44]

3.5 Magnetic properties

The temperature dependence of the magnetization $M(T)$ of LSSIRuO was characterized using a differential sample susceptometer under an applied magnetic field of 1 T, in both field-cooled (FC) mode (cooling under field) and zero-field-cooled (ZFC) mode (cooling without field), with a heating rate of 5 K per minute (Fig. 11).

The ferromagnetic isotropy is confirmed by the overlap of the magnetization curves M(FC) and M(ZFC), even at low temperatures. Paramagnetic behaviour is observed at high temperatures, and a second-order ferromagnetic–paramagnetic phase transition occurs around the Curie temperature of T_c = 155 K, as evidenced by the FC curve that does not exhibit a sharp change in slope when the temperature decreases to low temperatures. As shown in the inset of Fig. 11, the Curie temperature has been determined to be 155 K, corresponding to that at which the ZFC and FC curves begin to diverge when cooling the sample. The region where this occurs has been magnified (inset of Fig. 11).

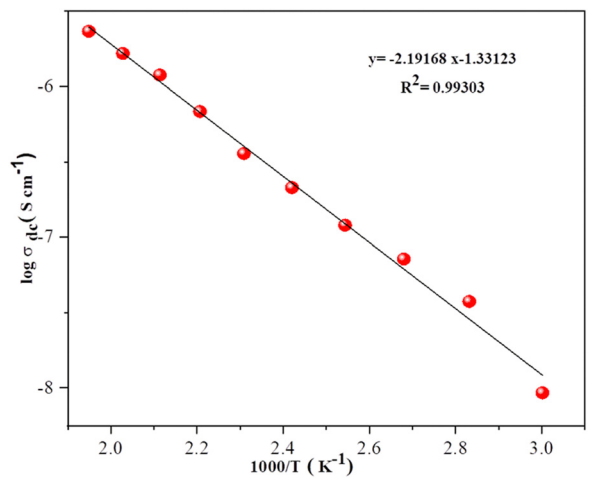

Fig. 10 The plot of DC conductivity as a function of temperature.

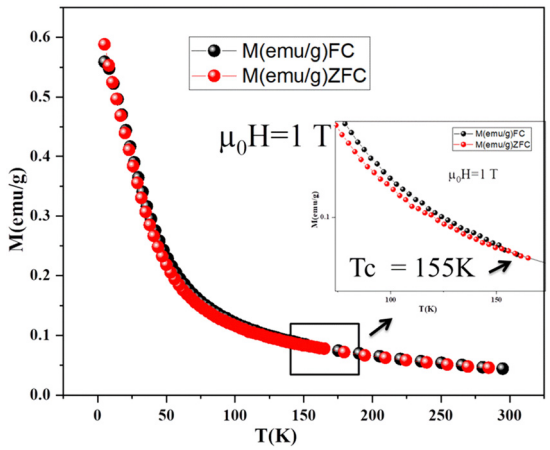

Fig. 11 Temperature dependence of the M(FC) and (ZFC) magnetization of LSSIRuO compound under $\mu_0 H$ = 1 T. (The inset shows the local enlargement where ZFC and FC curves begin to diverge.)

The magnetic hysteresis loops $M(H)$ of LSSIRuO powder at 8 K and 100 K are shown in Fig. 12 with an applied field reaching 10 T.

As the magnetic field increases, this compound undergoes a transition from a weak magnetic state to a strong one, it all depends on the applied field and temperature. The hysteresis loops exhibit a small area, highlighting the low energy loss during the magnetization–demagnetization process.[61] The parameters obtained from the curves are summarized in Table 4. As the temperature decreases, $\mu_0 H_C$ increases, and the ferromagnetic ordering becomes significantly enhanced. The value of M_R/M_S indicates a weak multi-domain structure in our case.

The occurrence of ferromagnetism in LSSIRuO, despite the diamagnetic nature of the mother compound SSO is intriguing. Various already known factors may contribute to the emergence of ferromagnetism in oxide-based semiconductors such as the incorporation of magnetic or mixed-valence ions,[62] as well as

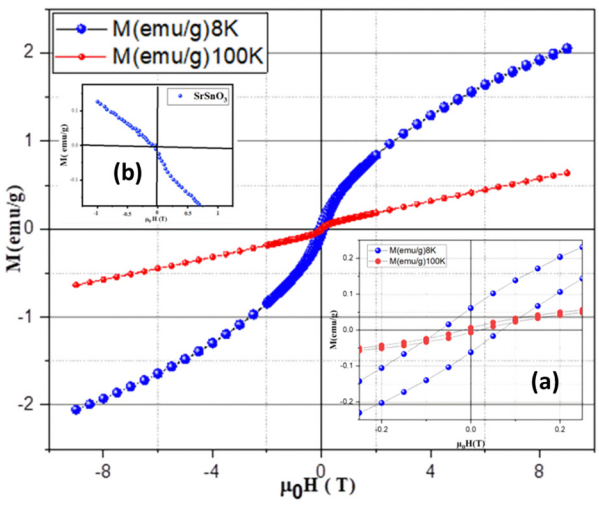

Fig. 12 Magnetization dependence of LSSIRuO as a function of the magnetic field. (Inset: (a) an enlarged view of the central region of the curves; (b) magnetisation of $SrSnO_3$.[60])

Table 4 Derived parameters from the M vs. ($\mu_0 H$) plots of the compound

T (K)	M_S (emu g^{-1})	M_R (emu g^{-1})	M_R/M_S	$\mu_0 H_C$ (T)
8	2.048	0.0623	0.0304	0.0724
100	0.63	0.0689	0.1093	0.0230

With M_S (saturation magnetization), M_R (remanence), and $\mu_0 H_C$ (coercive field).

the existence of magnetic impurities and defects.[63] However, at high doping concentrations, defects are likely to hinder the establishment of magnetic order.[5] This could explain the relatively low magnitude of ferromagnetism in our compound. Furthermore, the surface-level imperfections such as grain boundaries, deep point defects, and interstitials[5] are supposed to be absent and could not contribute to the observed ferromagnetism in our compound.

In our case, the observed ferromagnetism can only be explained by models involving free charge carriers, such as the Ruderman–Kittel–Kasuya–Yosida (RKKY) theory, superexchange, and double exchange interactions. According to the RKKY interaction theory, ferromagnetism arises from spin injection by the dopant, which interacts with the free electrons in the conduction band, inducing a ferromagnetic order.[60] In the superexchange interaction, each oxygen anion positioned between two Ru^{4+} ions in the Ru^{4+}–O–Ru^{4+} configuration leads to an antiferromagnetic order. Conversely, the order becomes ferromagnetic in the double exchange if this oxygen is situated in the Ru^{3+}–O–Ru^{4+} configuration, since Ru^{4+} is a magnetic ion with mixed valence.[62]

4. Conclusions

The $La_{0.25}Sr_{0.75}Sn_{0.4}In_{0.25}Ru_{0.35}O_3$ (LSSIRuO) compound has been successfully synthesized using a rapid, mild, effective, and reproducible mechanosynthesis method. This process resulted in an orthorhombic perovskite structure akin to $GdFeO_3$. XRD analysis confirmed the excellent crystallinity of the material, and the systematic doping of La, In, and Ru influenced the lattice constants. EDS analysis provided the chemical composition of each element, while IR spectroscopy validated the perovskite structure by identifying vibrational bands associated with LSSIRuO groups, such as SnO_6, RuO_6, and InO_6. The sample exhibited a significantly narrow band gap of 1.3 eV, as determined through diffuse reflection measurements. Intermediate energy states were identified as crucial for this band gap reduction. Additionally, LSSIRuO displayed substantially improved electrical conductivity compared to $SrSnO_3$, as evidenced by conductivity-as-a-function-of-temperature analysis, which indicated Arrhenius-type charge transport. Investigation into the magnetic properties, when doping $SrSnO_3$ with La, In and Ru, revealed a transition from dia- to ferromagnetic nature induced by superexchange and double exchange interactions. DFT predictions with an estimation of the band gap at the GGSA+U level of theory give a value of 1.55 eV, which agrees well with the experimentally obtained

value of 1.3 eV. It could be concluded that the increase in Ru doping favors the transition from the insulating state to the semiconductor state, then to the semi-metal/metal state. This chemical doping on both A and B sites demonstrates control over the functional properties, facilitating a transition from insulating to semi-metallic states and enabling exploration of optical, electrical, and magnetic properties. The highly reduced band gap, coupled with excellent electrical and magnetic characteristics, positions LSSIRuO as a promising candidate for optoelectronic, memory, and spintronic applications. Future applications in thin films aim to reveal the intricate interplay of these properties, further unveiling the semi-metallic ferromagnetic state.

Author contributions

Samira Barouni with Rached Ben Hassen carried out the synthesis, the powder XRD structure determination, the UV-vis, FTIR characterization and the electrical measurements of the material and participated in drafting the manuscript. Mikhail Maslov conducted the DFT calculations and drafted the corresponding section. Scanning electron microscopy and energy-dispersive X-ray analysis were carried out by Akram Alhussein. Magnetic measurements were conducted by Hanen Chaker. Amani Brahmia participated in the powder XRD structure determination and FTIR characterization. Revision and editing were performed by Rached Ben Hassen, Mikhail Maslov and Samira Barouni. All authors read and approved the final manuscript.

Conflicts of interest

There are no conflicts to declare.

Acknowledgements

The authors gratefully acknowledge the ICDD for the financial support (grant number: 09-04) and extend their appreciation to the Deanship of Research and Graduate Studies at King Khalid University for funding this work through a Large Research Project under grant number RGP2/53/45.

Notes and references

1 O. V. Nkwachukwu and O. A. Arotiba, *Front. Chem.*, 2021, **9**, 634630.
2 A. Kostopoulou, K. Brintakis, N. K. Nasikas and E. Stratakis, *Nanophotonics*, 2019, **8**(10), 1607–1640.
3 M. S. Hossain and A. Takshi, *MRS Adv.*, 2021, **6**, 645–649.
4 B. Belgacem, M. M. Maslov, S. Kaya, I. H. Ali and R. Ben Hassen, *J. Mol. Struct.*, 2022, **1259**, 132716.
5 M. Avinash, M. Muralidharan, S. Selvakuma, S. Selvakumar and K. Sivaji, *J. Mater. Sci.: Mater. Electron.*, 2020, **31**(4), 3375–3386.
6 K. P. Ong, X. Fan, A. Subedi, M. B. Sullivan and D. J. Singh, *APL Mater.*, 2015, **3**(6), 062505.
7 Y. Kumar, R. Kumar, R. J. Choudhary, A. Thakur and A. P. Singh, *Ceram. Int.*, 2020, **46**(11), 17569–17576.
8 M. M. Kumar, P. Singh, D. Kumar and O. Parkash, *Adv. Appl. Ceram.*, 2006, **105**(6), 280–284.
9 S. Ouni, S. Nouri, J. Rohlicek and R. Ben Hassen, *J. Solid State Chem.*, 2012, **192**, 132–138.
10 A. Kumar, V. Sahrawat, A. A. Kumar and S. Priya, *Trans. Indian Inst. Met.*, 2017, **70**(3), 573–579.
11 Q. Gao, K. Li, L. Zhao, K. Zhang, H. Li, J. Zhang and Q. Liu, *ACS Appl. Mater. Interfaces*, 2019, **11**, 25605–25612.
12 S. Halder, R. A. Kumar, R. Maity and T. P. Sinha, *Ceram. Int.*, 2023, **49**(5), 8634–8645.
13 A. Malešević, A. Radojković, M. Žunić, S. M. Savić, S. Perać, Z. Branković and G. Branković, *Ceram. Int.*, 2023, **49**(10), 15673–15679.
14 W. Ming, H. Shi and M.-H. Du, *J. Mater. Chem.*, 2016, **4**(36), 13852–13858.
15 Y. Zhou, H. F. Garces, B. S. Senturk, A. L. Ortiz and N. P. Padture, *Mater. Lett.*, 2013, **110**, 127–129.
16 M. Wang, W. Wang, B. Ma, W. Shen, L. Liu, K. Cao, S. Chen and W. Huang, *Nano-Micro Lett.*, 2021, **13**(1), 62.
17 M. I. Katsnelson, V. Y. Irkhin, L. Chioncel, A. I. Lichtenstein and R. A. de Groot, *Rev. Mod. Phys.*, 2008, **80**(2), 315–378.
18 P. A. Lin, H. T. Jeng and C. S. Hsue, *Phys. Rev. B: Condens. Matter Mater. Phys.*, 2008, **77**(8), 085118.
19 J. Kim, J. Y. Kim, B. G. Park and S. J. Oh, *Phys. Rev. B: Condens. Matter Mater. Phys.*, 2006, **73**(23), 235109.
20 N. Kim, R. Kim and J. Yu, *J. Magn. Magn. Mater.*, 2018, **460**, 54–60.
21 A. Huon, S. Yoon, M. R. Fitzsimmons, T. R. Charlton, J. M. Ok, C. D. Cruz and H. N. Lee, *Appl. Phys. Lett.*, 2021, **119**, 112404.
22 K. W. Lee and K. H. Ahn, *Phys. Rev. B: Condens. Matter Mater. Phys.*, 2012, **85**(22), 224404.
23 K. I. Kobayashi, T. Kimura, H. Sawada, K. Terakura and Y. Tokura, *Nature*, 1998, **395**(65), 677–680.
24 J. R. Carvajal, *FULLPROF Program for Rietveld Refinement*, Laboratorie Leon Brillouin, CEA Saclay, France, 2000.
25 P. Giannozzi, S. Baroni, N. Bonini, M. Calandra, R. Car, C. Cavazzoni, D. Ceresoli, G. L. Chiarotti, M. Cococcioni and I. Dabo, *J. Phys.: Condens. Matter*, 2009, **21**, 395502.
26 P. Giannozzi, O. Andreussi, T. Brumme, O. Bunau, M. B. Nardelli, M. Calandra, R. Car, C. Cavazzoni, D. Ceresoli, M. Cococcioni, N. Colonna, I. Carnimeo, A. D. Corso, S. de Gironcoli, P. Delugas, R. A. DiStasio Jr, A. Ferretti, A. Floris, G. Fratesi, G. Fugallo, R. Gebauer, U. Gerstmann, F. Giustino, T. Gorni, J. Jia, M. Kawamura, H. Y. Ko, A. Kokalj, E. Küçükbenli, M. Lazzeri, M. Marsili, N. Marzari, F. Mauri, N. L. Nguyen, H. V. Nguyen, A. O. de la Roza, L. Paulatto, S. Poncé, D. Rocca, R. Sabatini, B. Santra, M. Schlipf, A. P. Seitsonen, A. Smogunov, I. Timrov, T. Thonhauser, P. Umari, N. Vast, X. Wu and S. Baroni, *J. Phys. Condens. Matter*, 2017, **29**(46), 465901.
27 J. P. Perdew, K. Burke and M. Ernzerhof, *Phys. Rev. Lett.*, 1996, **77**(18), 3865–3868.

28 G. Prandini, A. Marrazzo, I. E. Castelli, N. Mounet and N. Marzari, *npj Comput. Mater.*, 2018, **4**(1), 72.
29 E. Küçükbenli, Y. O. Kvashnin, I. L. M. Locht, S. Lubeck, M. Marsman, N. Marzari, U. Nitzsche, L. Nordström, T. Ozaki, L. Paulatto, C. J. Pickard, W. Poelmans, M. I. J. Probert, K. Refson, M. Richter, G. M. Rignanese, S. Saha, M. Scheffler, M. Schlipf, K. Schwarz, S. Sharma, F. Tavazza, P. Thunström, A. Tkatchenko, M. Torrent, D. Vanderbilt, M. J. van Setten, V. Van Speybroeck, J. M. Wills, J. R. Yates, G. X. Zhang and S. Cottenier, *Science*, 2016, **351**(6280), 1415-U81.
30 P. E. Blöchl, O. Jepsen and O. K. Andersen, *Phys. Rev. B: Condens. Matter Mater. Phys.*, 1994, **49**(24), 17953–17979.
31 G. Kresse and D. Joubert, *Phys. Rev. B: Condens. Matter Mater. Phys.*, 1999, **59**, 1758–1775.
32 V. I. Anisimov, J. Zaanen and O. K. Andersen, *Phys. Rev. B: Condens. Matter Mater. Phys.*, 1991, **44**(3), 943–954.
33 V. I. Anisimov, I. V. Solovyev, M. A. Korotin, M. T. Czyżyk and G. A. Sawatzky, *Phys. Rev. B: Condens. Matter Mater. Phys.*, 1993, **48**(23), 16929–16934.
34 M. Cococcioni and S. de Gironcoli, *Phys. Rev. B: Condens. Matter Mater. Phys.*, 2005, **71**(3), 035105.
35 H. J. Monkhorst and J. D. Pack, *Phys. Rev. B: Solid State*, 1976, **13**(12), 5188–5192.
36 M. Methfessel and A. T. Paxton, *Phys. Rev. B: Condens. Matter Mater. Phys.*, 1989, **40**(6), 3616–3621.
37 P. E. Blöchl, O. Jepsen and O. K. Andersen, *Phys. Rev. B: Condens. Matter Mater. Phys.*, 1994, **49**(23), 16223–16233.
38 J. W. Song, K. Yamashita and K. Hirao, *J. Chem. Phys.*, 2011, **135**, 071103.
39 J. Heyd, G. E. Scuseria and M. Ernzerhof, *J. Chem. Phys.*, 2003, **118**(18), 8207–8215.
40 V. M. Goldschmidt, *Naturwissenschaften*, 1926, **14**(21), 477–485.
41 W. Li, E. Ionescu, R. Riedel and A. Gurlo, *J. Mater. Chem. A*, 2013, **1**(39), 12239.
42 C. J. Bartel, C. Sutton, B. R. Goldsmith, R. Ouyang, C. B. Musgrave, L. M. Ghiringhelli and M. Scheffler, *Sci. Adv.*, 2019, **5**(2), eaav0693.
43 R. D. Shannon, *Acta Crystallogr., Sect. A: Cryst. Phys., Diffr., Theor. Gen. Crystallogr.*, 1976, **32**(5), 751–767.
44 S. Ouni, S. Nouri, J. Rohlicek and R. Ben Hassen, *J. Solid State Chem.*, 2012, **192**, 132–138.
45 O. C. Gagné and F. C. Hawthorne, *Acta Crystallogr., Sect. B: Struct. Sci., Cryst. Eng. Mater.*, 2018, **74**(1), 63–78.
46 O. C. Gagné and F. C. Hawthorne, *IUCrJ*, 2020, **7**, 581–629.
47 H. Mizoguchi, H. W. Eng and P. M. Woodward, *Inorg. Chem.*, 2004, **43**(5), 1667–1680.
48 M. O'keeffe and B. G. Hyde, *Acta Crystallogr., Sect. B: Struct. Crystallogr. Cryst. Chem.*, 1977, **33**(12), 3802–3813.
49 A. Cammarata and J. M. Rondinelli, *J. Chem. Phys.*, 2014, **141**(11), 114704.
50 W. Hume-Rothery and G. V. Raynor, The Structure of Metals and Alloys, Institute of Metals Monograph and Report Series, 1962, No. 1, pp. 210–217.
51 W. D. Kingery, H. K. Bowen and D. R. Uhlmann, *Introduction to ceramics*, Wiley, 1976.
52 A. Zouaghi, B. Belgacem, A. Alhussein, A. Brahmia and R. Ben Hassen, *J. Solid State Chem.*, 2023, **328**, 124303.
53 M. B. Khanvilkar, A. K. Nikumbh, R. A. Pawar, N. J. Karale, D. V. Nighot, R. C. Ambare, P. A. Nagwade, M. D. Sangale, G. S. Gugale and S. B. Misal, *Phys. Chem. Solid State*, 2021, **22**(4), 664–686.
54 M. C. F. Alves, M. R. Nascimento, S. J. G. Lima, P. S. Pizani, J. W. M. Espinosa, E. Longo, L. E. B. Soledade, A. G. Souza and L. M. G. Santos, *Mater. Lett.*, 2008, **63**(1), 118–120.
55 R. A. Nyquist and R. O. Kagel, *Infrared Spectra Atlas of Inorganic Compounds*, Academic Press, 1971.
56 J. Hong, S. J. Heo and P. Singh, *Sci. Rep.*, 2021, **11**, 3368.
57 R. Malik, V. K. Tomer, S. Duhan, S. P. Nehra and P. S. Rana, *Energy Environ. Focus*, 2015, **4**(4), 340–345.
58 T. Mohan, S. Kuppusamy and R. J. V. Michael, *ACS Omega*, 2022, **7**(22), 18531–18541.
59 A. Kumar, B. Khan, V. Yadav, A. Dixit, U. Kumar and M. K. Singh, *J. Mater. Sci.: Mater. Electron.*, 2020, **31**, 16838–16848.
60 M. Muralidharan, V. Anbarasu, A. Elaya Perumal and K. Sivakumar, *J. Mater. Sci.: Mater. Electron.*, 2016, **28**(5), 4125–4137.
61 N. Amri, J. Massoudi, K. Nouri, M. Triki, E. Dhahri and L. Bessais, *RSC Adv.*, 2021, **11**(22), 13256–13268.
62 J. M. D. Coey, M. Venkatesan and C. B. Fitzgerald, *Nat. Mater.*, 2005, **4**(2), 173–179.
63 J. M. D. Coey, K. Wongsaprom, J. Alaria and M. Venkatesan, *J. Phys. D: Appl. Phys.*, 2008, **41**(13), 134012.

